We are IntechOpen, the world's leading publisher of Open Access books Built by scientists, for scientists

4,800
Open access books available

122,000
International authors and editors

135M
Downloads

Our authors are among the

154
Countries delivered to

TOP 1%
most cited scientists

12.2%
Contributors from top 500 universities

WEB OF SCIENCE™

Selection of our books indexed in the Book Citation Index in Web of Science™ Core Collection (BKCI)

Interested in publishing with us?
Contact book.department@intechopen.com

Numbers displayed above are based on latest data collected.
For more information visit www.intechopen.com

8

Advantages of a Programmed Surface Designed by Organic Monolayers

Naoto Shirahata
National Institute for Materials Science (NIMS), Sengen, Tsukuba, Ibaraki, Japan

1. Introduction

Increasing attention has been paid to the control over surface chemical property of bare metals, semiconductors, ceramics, and polymers in the development of nanoscience and nanotechnology. The appropriate functionalization has a potential to lead to the appearance of new function. Organic monolayers, i.e., self-assembled monolayers (SAMs), are simple monomolecular system, convenient, and flexible to tailor the substrate's surface chemical and physical properties including wetting property, conductivity, and thermal, chemical, photochemical stabilities, etc. In the following molecular diagram of organic monolayers, its molecular anatomy and characteristics are highlighted as shown in Figure 1. Such monolayer structures are formed by chemisorption of organic constituents onto the specific solid substrate through liquid or gas phase. A headgroup of the organic constituent reacts to the outermost atoms on the substrate to give a chemical linkage. The chemisorbates organize epitaxially to form crystalline monomolecular film structures. As shown in the molecular

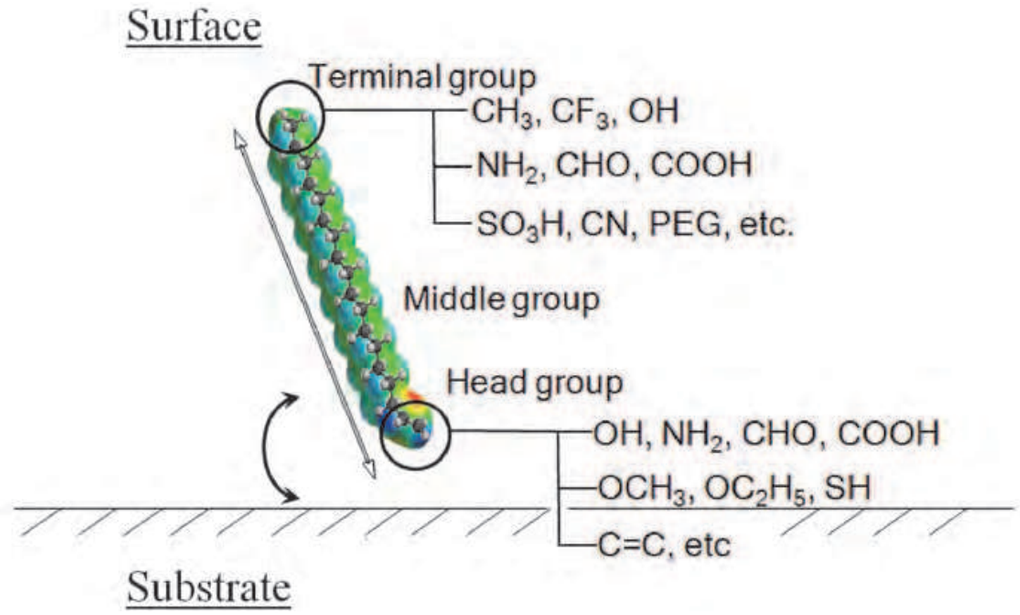

Fig. 1. Schematic diagram of organic monolayers formed on solid substrates

diagram, there is a number of headgroups which can recognize the outermost chemical groups of substrates, resulting in a chemical bond. In contrast, there is no limitation in the selection of terminal functional groups. A wide variety of functionalities or reactivities are applicable. A lateral molecular space, which is controlled by hydrophobic molecular interaction between hydrocarbon chains, allows the control of the film crystallinity and electron transferring behavior between the terminal group and substrate surface. Thus, programmed surface can be designed by careful control of monolayer attachment. Since the finding of siloxane SAM structure in 1980, a number of research efforts have been performed. In this review article, organic monolayer systems on polymer and silicon substrates are focused, and their potential applications is also demonstrated.

2. Chemical modification of a polymer surface

2.1 Motivation

Recently, the deposition of inorganic materials, e.g., ceramics, metals, and semiconductors, has interestingly attracted attention in the development of mechanically-flexible device applications including OLED, flexible flat panel and wearable displays, electronic papers, biomedical tools. These technological developments take advantage of polymer's excellent properties including mechanical flexibility, lightweight, ease-of-design and coloring, low-cost and good impact resistance. In order to fabricate such flexible device applications, it is a key to control chemical properties of polymer's surface that induce the nucleus formation of inorganic crystals, and accelerates subsequent crystalline growth or film growth. Organosilane SAMs have been frequently employed to modify surface chemically properties of inorganic substrates [1-5]. The resultant surfaces play important roles in molecular recognition events. For example, some of functional groups induce the nucleus formation of inorganic crystals, and accelerates subsequent crystalline growth or film growth. This section describes the preparation of well-ordered SAM structures on polymer sheet, and then the deposition of metal and ceramics films on the SAM-covered polymer sheets through solution processes.

2.2 SAM formation

When silane molecules are treated directly on as-received polymer sheet, they cannot form a monomolecular structure. Similar can be seen even on photochemically treated polymer sheet. In other words, when silane precursors are directly treated on surface-activated polymer substrates, well-ordered SAM formation cannot effectively proceed, since the polar-functional groups formed on a polymer surface through surface modification methods using plasma or UV light are generally inhomogeneous and randomly distributed [5]. Such a heterogeneous surface cannot provide adequate support for the preparation of a well-ordered SAM. As an example, Table 1 summarizes the contact angles and surface free energies of polyimide surfaces covered with NH_2- and CF_3-terminated SAMs, and their values are compared with those of SAM-covered silicon substrates used as standards. The formation of the SAMs is performed on photooxidized polyimide and silica-covered silicon substrates, respectively. The details of the SAM preparation method are described in elsewhere [5], but the surface energies of each sample are calculated using the following equation:

$$\gamma_L(1+\cos\theta_S{}^L) = 2[(\gamma_s{}^d \bullet \gamma_L{}^d)^{1/2} + (\gamma_s{}^P \bullet \gamma_L{}^P)^{1/2} + (\gamma_s{}^h \bullet \gamma_L{}^h)^{1/2}]$$

where γ_L is the liquid's surface energy, and θ_S^L is its contact angle on the solid surface. The superscripts d, p, and h indicate the dispersion, polar and hydrogen bonding forces, respectively. Since the γ_L, γ_L^d, γ_L^P, and γ_L^h values of the three liquids are known (i.e., for water, γ_L = 72.8 mN/m, γ_L^d= 29.1 mN/m, γ_L^P = 1.3 mN/m, and γ_L^h = 42.4 mN/m; for methylene iodide, γ_L = 50.8 mN/m, γ_L^d= 46.8 mN/m, γ_L^P = 4.0 mN/m, and γ_L^h = 0 mN/m; and for *n*-decane, γ_L = 23.9 mN/m, γ_L^d= 23.9 mN/m, γ_L^P = 0 mN/m, and γ_L^h = 0 mN/m), the surface free energy (γ_S) of the sample is estimated to be the sum of the calculated γ_S^d, γ_S^P, and γ_S^h values.

	SAM on SiO_2/Si	SAM on Polyimide (PI_{ox})
FAS-SAM: $CF_3(CF_2)_7(CH_2)_2Si(OCH_3)_3$		
θ_c	= 115°	= 107°
γ_s	= 11.9 mN/m	= 27.4 mN/m
γ_s^d	= 11.7 mN/m	= 13.2 mN/m
γ_s^p	= 0.1 mN/m	= 14.2 mN/m
γ_s^h	= 0.1 mN/m	= 0.0 mN/m
AHAPS-SAM: $H_2N(CH_2)_6NH(CH_2)_3Si(OCH_3)_3$		
θ_c	= 60.0°	= 69.6°
γ_s	= 61.9 mN/m	= 45.2 mN/m
γ_s^d	= 23.9 mN/m	= 23.9 mN/m
γ_s^p	= 26.2 mN/m	= 13.1 mN/m
γ_s^h	= 11.8 mN/m	= 8.2 mN/m

Table 1. Surface free energies of SAM-covered photooxidized polyimide (PI), i.e., PI_{ox}, and are compared with those of standard, i.e., SAM-covered SiO_2/Si.

Let's see the impact direct formation of FAS-SAM onto PI_{ox}, i.e., photooxidized polyimide, will have its intermolecular structure. The water contact angle of the FAS/PI_{ox} surface is somewhat smaller than that of the standard sample, that is, FAS-SAM/SiO_2/Si, but high hydrophobic character can be seen even on it. However, this small difference in surface hydrophobicity influences strongly on the crystal growth behavior of metal oxide film, as described later. The reason why small difference in wetting property occurs between the surfaces can be well understood by comparison of surface free energy of the sample with that of the standard. As shown in Table 1, the γ_S value of the FAS/PI_{ox} substrate (27.4 mN/m) is twice larger than that of a FAS/SiO_2/Si substrate (11.9 mN/m). This indicates that the molecular density of the FAS-SAM attached to the PI_{ox} surface is considerably low compared to the reference substrate. In particular, the γ_S^P value of the FAS/PI_{ox} substrate (14.2 mN/m) is much larger than that of the FAS/SiO_2/Si substrate (0.1 mN/m). This clearly demonstrates that the PI_{ox} surface underneath the FAS layer is probably exposed to air to some extent. It can be concluded that the degree of surface coverage by the FAS molecules differ greatly between the PI_{ox} and SiO_2/Si substrates. In the sample covered with an amine group, its static-water contact angle is estimated about 69.6° which is slightly larger than that of the reference sample. This small increase can be also discussed comparing

surface free energies between sample and reference. The γ_S value (45.2 mN/m) is approximately three-fourths of that calculated for the standard, and , is slightly larger than that of a surface terminated with CH_2 groups (36 mN/m). Both γ_S^d and γ_S^h values are consistent with those of standard, but the γ_S^P value of the AHAPS/PI_{ox} substrate (13.1 mN/m) is almost half of those obtained for the AHAPS/SiO_2/Si substrates (26.2 mN/m). These experimental results suggest that the degree of surface molecular coverage is much less than those on the reference surfaces. As a result, such heterogeneous surfaces cannot provide adequate support for the preparation of well-ordered SAMs. Chemical templates consisting of such disordered SAMs are considered to be unfavorable for the deposition of inorganic materials on polymer substrates. Furthermore, after a relatively short time, such disordered moieties will lose their functionalities, resulting in a decrease of surface activity on the modified polymeric surface. Thus, to avoid hydrophobic recovery, SAM fabrication must be conducted immediately after surface photooxidation. Otherwise it is difficult to form covalent bonds between the SAM and the polymer surface, resulting in weak adhesion. Thus, in spite of polymer substrates offering the attractive advantages described above, such obstacles may prevent the preparation of high quality SAMs.

To overcome this shortcoming, this section demonstrates the formation of a well-ordered SAMs on PI sheets through the chemisorption of organosilane molecules at the solid/vapor interface. PI has been utilized primarily as a substrate for printed circuit boards due to its excellent thermal stability, mechanical strength and insulating properties. In the present study, in order to give silica-like properties to the PI surface, we fabricated an ultrathin buffer layer on the substrates using a either one of precursor vapors of tetraethoxysilane (TEOS) or 1,3,5,7-tetramethylcyclotetrasiloxane (TMCTS) prior to forming the SAM. Let's focus on the effects of this buffer layer on the quality of the obtained SAMs. Well-ordered SAM structures are formed on PI surfaces according to the process illustrated in Figure 2. In the first step Figure 8a), a commercial PI sheet is photochemically hydrophilized to give a PI_{ox} surface. Due to this photoirradiation, the PI surface becomes completely hydrophilic with its water-contact angle dropping from about 71° to 5° or less. In the next step (Figure 2b), either one of organosilane molecules is chemisorbed onto the PI_{ox} surface. The PI_{ox} sheet is placed together with a glass cup filled with 0.2 cm^3 TMCTS (or TEOS) into a 65 cm^3 $Teflon_{TM}$ container in a dry N_2 atmosphere with less than 10% relative humidity. The container is sealed with a cap and heated in an oven maintained at 80°C for 3 h. Next, in order to convert the chemisorbed TMCTS (or TEOS) molecule into an ultrathin SiO_2 layer, the sample is again irradiated for 30 min in a manner similar to the PI surface modification mentioned above. Finally, a SAM is formed on the SiO_2-covered PI_{ox} surface through a vapor phase (Figure 2e). The thickness of the SiO_2 nanolayer formed on the PI_{ox} substrate is estimated from a cross-sectional image acquired by HR-TEM, as shown in Figure 3. As clearly indicated by the arrows, an extremely thin layer is found to form on the PI_{ox} substrate, as a black contrasted image. Two important things can be seen in this cross-sectional view. One is that the ultrathin layer uniformly deposits over the entire surface of the PI_{ox}. There are no defects such as a void and a pinhole. The other is an actual thickness of this layer which is estimated from this image to be only 1 nm or less. As confirmed by XPS, the binding energy of the Si2p spectrum for this sample is located at 103.6 eV, the value of which is consistent with that of a Si substrate covered with native oxide (SiO_2/Si, 103.6 eV). Therefore, the nanolayer undoubtedly formed on the PI_{ox} substrate. Due to this SiO_2 nanolayer coating, the surface chemical properties of the PI substrate are expected to be the same as those of SiO_2/Si substrates, as evidenced in Table 2. In the case of the

SAM/nanolayer/PI_{ox} sample, a highly oriented SAM is expected to have grown similarly on the substrate. Unlike SAM sample without SiO_2 nanolayer (see Table 1), the γ_S values of the SAM-covered PI_{ox} samples (12.4 mN/m for FAS and 62.8 mN/m for AHAPS) are almost consistent with those of the standard substrate (11.9 mN/m for FAS and 61.9 mN/m for AHAPS). Specifically, the SAM formation on the nanolayer leads to the γ_S^P which nearly corresponds to the value on the reference sample. As a result, this nanolayer opens SAM chemistry even on polymer sheet [5,6].

SAM on SiO_2/Si	SAM/Nanolayer/PI_{ox}
FAS-SAM: $CF_3(CF_2)_7(CH_2)_2Si(OCH_3)_3$	
θ_c = 115°	θ_c = 115°
γ_S = 11.9 mN/m	γ_S = 12.4 mN/m
γ_S^d = 11.7 mN/m	γ_S^d = 12.2 mN/m
γ_S^p = 0.1 mN/m	γ_S^p = 0.1 mN/m
γ_S^h = 0.1 mN/m	γ_S^h = 0.1 mN/m
AHAPS-SAM: $H_2N(CH_2)_6NH(CH_2)_3Si(OCH_3)_3$	
θ_c = 60.0°	θ_c = 61.4°
γ_S = 61.9 mN/m	γ_S = 62.8 mN/m
γ_S^d = 23.9 mN/m	γ_S^d = 23.9 mN/m
γ_S^p = 26.2 mN/m	γ_S^p = 28.5 mN/m
γ_S^h = 11.8 mN/m	γ_S^h = 10.4 mN/m

Table 2. Surface free energies of SAMs on SiO_2 nanolayer/PI_{ox} substrates, and are compared with those of standard, i.e., SAM-covered SiO_2/Si.

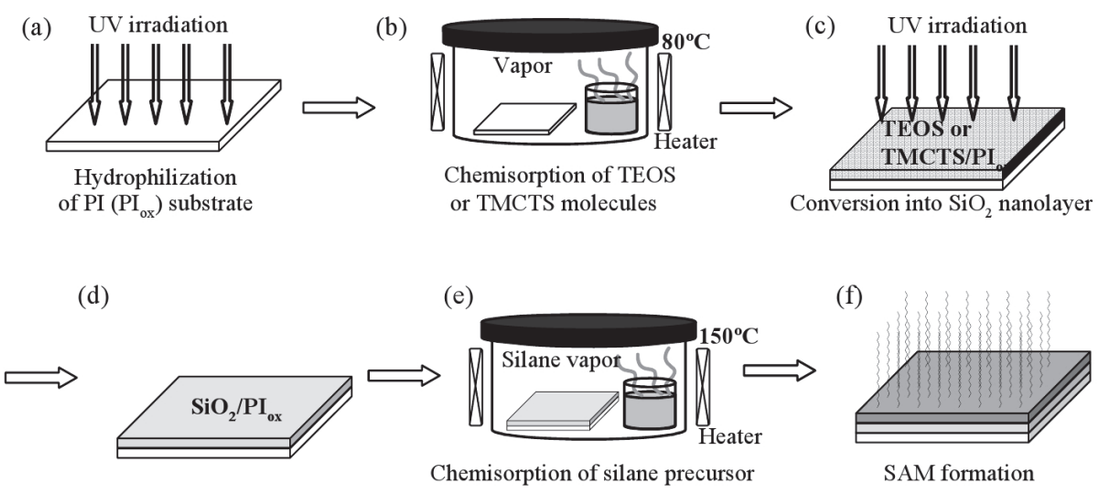

Fig. 2. Schematic diagram for SAM formation on PI_{ox} substrate with a 1 nm thick SiO_2 buffer layer.

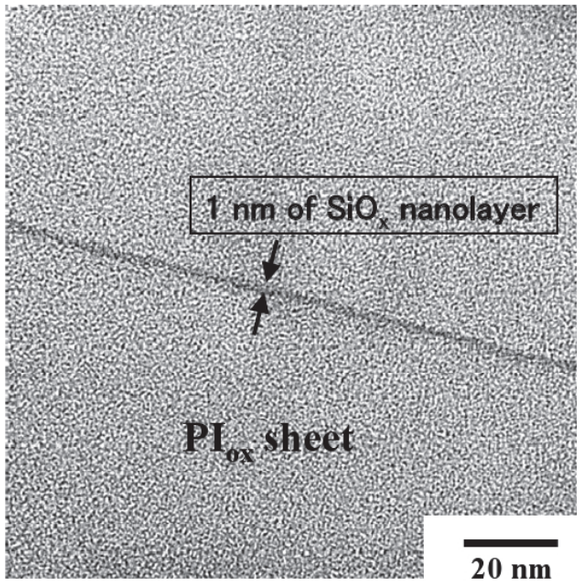

Fig. 3. A cross-sectional HR-TEM image of TEOS-covered PI_{ox} substrate after photooxidation. The TEOS layer is converted into 1 nm thick silica layer as a consequence of the photooxidation with vacuum UV light at 10^3 Pa.

2.3 Attachment of ceramics film on polyimide

This subsection describes the potentials as chemical templates of SAMs formed on nanolayers in the deposition of metal and ceramics from liquid phase. To achieve a better understanding of the potentials, SAM-covered samples with and without silica nanolayer are micropatterned by photoirradiation with UV lamp through photomasks.

Among the various types of reactive functional groups, amino groups are of particular interest owing to their chemical reactivities. Palladium colloid is particularly important as a catalyst for the fabrication of metal micropatterns on non-conductive substrates like a polymer. Figure 4 illustrates a deposition process of copper microlines on polymer sheets with and without a silica nanoalyer. Each of SAM-covered PI_{ox} sheets are photolithographically micropatterned (Figure 4a). The micropatterned sample substrates are activated for 20~30 min by immersion in a Pd(II) solution containing $PdCl_2$ and HCl (adjusted to pH 5.0 by adding aq-NaOH solution), followed by gentle rinsing with Milli-Q water (Figure 4c). These activated substrates are then immediately immersed in a commercial plating bath containing formaldehyde as a reducing agent (Figure 4d). The pH value of this solution is 12.5. As a result, copper microlines are deposited on the AHAPS chemical templates, as shown in Figure 4e. The comparison of LFM images (a) with (b) in Figure 5 shows the significant difference in a quality of SAMs formed on PI_{ox} with (b) and without (a) nanolayer. In these LFM images, bright and dark areas correspond to photoirradiated and unirradiated regions, respectively. As can be seen in Figure 5b, the 10-μm-wide micropatterns are clearly imaged through the friction force contrast between the photoirradiated and masked regions of the AHAPS/nanolayer/PI_{ox} substrate. The photoirradiated regions exhibit stronger friction forces than the unirradiated AHAPS-covered regions. Due to UV irradiation, an AHAPS-SAM is removed through oxidation with UV-activated oxygen species. Accordingly, in the UV-irradiated regions of the sample, the bottom part of the AHAPS layer, which consisted of a 0.2~0.27 nm-thick SiO_2 monolayer,

remains on the ONS/PI_{ox} substrate surface. This SiO_2 monolayer-covered nanolayer/PI_{ox} surface is highly hydrophilic with a water-contact angle of 5° or less. It therefore adheres more strongly to the Si probe surface, which is also covered with a hydrophilic native SiO_2 layer. The friction force contrast on the UV-irradiated regions is thus greater than that on the AHAPS-covered areas. Although it can be expected that this SiO_2 monolayer would similarly remain on the UV-irradiated regions of the AHAPS/PI_{ox} substrate, the friction force contrast in its LFM image (Figure 5a) is relatively small compared to that of the AHAPS/nanolayer/PI_{ox} substrate. In addition, several dark areas can be observed, even in the SiO_2 monolayer-covered regions. This reveals that areas of weak friction exist on the

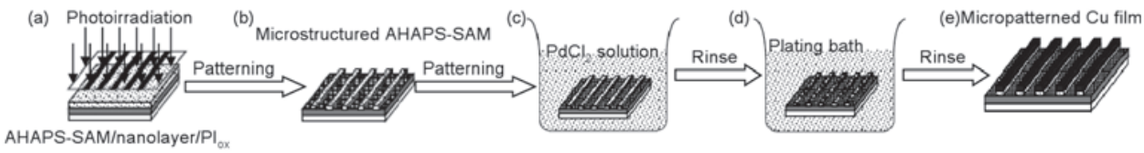

Fig. 4. Schematic illustration showing the fabrication of copper microlines on PI_{ox} substrate.

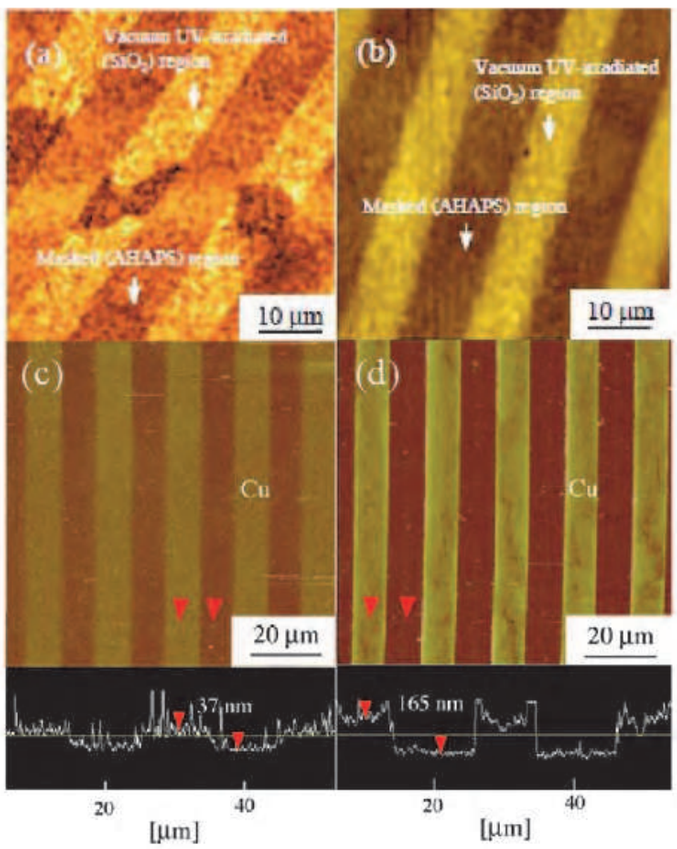

Fig. 5. LFM images of micropatterned PI_{ox} substrates covered with (a) AHAPS-SAM and (b) AHAPS-SAM/nanolayer, and AFM images and their cross-sectional views of copper microlines area-selectively electroless plated on the micropatterned (c) AHAPS-SAM/PIox and (d) AHAPS-SAM/nanolayer/PI_{ox} substrates.

SiO_2 monolayer-covered regions. These are believed to be due to incomplete termination with AHAPS molecules. As mentioned in the previous section, since the packing density of the AHAPS molecules on the PI_{ox} substrate is considered to be low, parts of the PI_{ox} substrate surface which does not react with AHAPS molecule probably remain even after its SAM formation. However, the polar-functional groups terminating such a surface are unstable and gradually lose their polarity due to hydrophobic recovery, resulting in a decrease in hydrophilicity of the PI_{ox} surface. The dark regions are considered to be hydrophobic areas regenerated by this hydrophobic recovery.

Copper films are deposited on both micropatterned samples, since both the amount of Pd catalyst adsorbed and the subsequent growth of Cu through electroless plating are thought to be related to the termination states of the NH_2 groups in the AHAPS molecules. Typical AFM images of the electroless-plated copper microlines and their schematic cross-sections on both micropatterned AHAPS/PI_{ox} and AHAPS/nanolayer/PI_{ox} substrates are shown in Figures 5c and d, respectively. In both images, continuous film-like deposits of Cu can be seen on the masked regions, while the surrounding photoirradiated regions remain free of deposits. 10-μm-wide Cu microlines are successfully formed in a 10×10 μm^2 area on both substrates. The film thicknesses as estimated from these images are about 37 and 165 nm for Figures 5c and d, respectively. Accordingly, the growth rate of each is calculated to be about 3.7 and 16.5 nm/min, respectively, because of the deposition time of a 10 min in both cases. It is clear that the electroless Cu plating proceeded more efficiently on the AHAPS/nanolayer/PI_{ox} substrate. Its Cu growth rate is roughly consistent with that observed on an AHAPS/SiO_2/Si substrate (20 nm/min or less). In spite of the fact that immersion time is identical, the growth rate on the AHAPS/PI_{ox} substrate without the silica buffer layer is only about one-fifth of that on the AHAPS/nanolayer/PI_{ox} substrate, offering further proof that the degree of surface coverage by Pd catalyst particles is much higher on the AHAPS/nanolayer/PI_{ox} substrate than on the AHAPS/PI_{ox} substrate. As with the plating rate, the pattern resolution also depends on the quality of the AHAPS-SAM. As clearly seen in the cross-section of the Cu microlines on the AHAPS/nanolayer/PI_{ox} substrate (Figure 5d), the edge regions are relatively sharp. On the contrary, the microlines' edge sharpness is low on the AHAPS/PI_{ox} substrate (Figure 5c). These results agree well with the LFM results described above. It is thus concluded that the silica interlayer proves effective in fabricating a well-defined AHAPS-SAM even on a polymer substrate, in a manner similar to that seen on a SiO_2/Si substrate. In addition, the micropatterned substrate prepared by the present approach serves as an ideal template for spatially defined electroless Cu plating on nonconductive polymer substrate.

Next, the role of a high quality chemical template for depositing ceramics film, i.e., tin oxide, is demonstrated. The FAS-covered samples with and without silica nanolayer are photolithographycally micropatterned as shown in Figure 6a. Each patterned samples is immersed into a 1 M HCl solution containing 0.05 mol/l of $SnCl_2 \cdot 2H_2O$ (see Figure 6b). After immersion, the substrates are immediately washed with Milli-Q water several times, blown dry with N_2 gas, and subsequently sonicated for 0.5~2.0 h in absolute toluene (Figure 6c) to remove the deposits from FAS-covered regions. We named this "solution lithography" [1]. As a result, a microstructured tin oxide film is obtained (Figure 6d). Typical optical micrographs of the films deposited on both the micropatterned FAS/nanolayer/PI_{ox} and FAS/PI_{ox} substrates (deposition time of 24 h; sonication time of 2 h) are shown in Figures 7a and 7b, respectively. As can be seen in Figure 7a, tin oxide deposits with continuous film-like features remain on the photoirradiated regions, while the

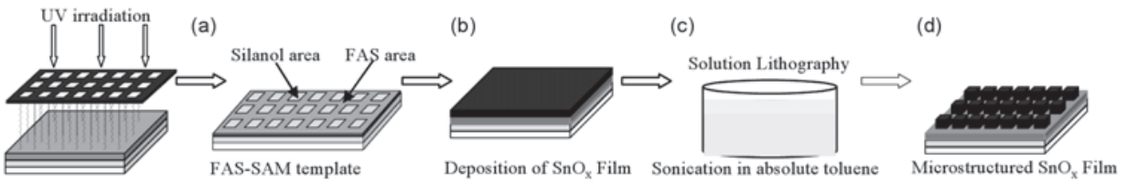

Fig. 6. Schematic illustration showing the microfabrication process of metal oxide film on PI_{ox} substrate.

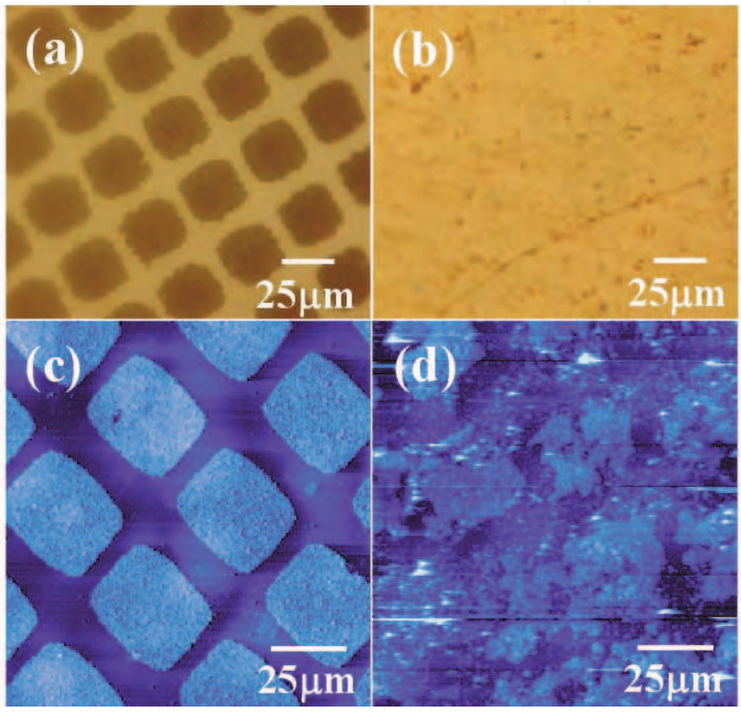

Fig. 7. Optical (a and b) and DFM images (c and d) of tin oxide film microstructured on two different substrates: (a), (c) on FAS/nanolayer/PI_{ox} substrate, while (b), (d) on FAS/PI_{ox} substrate, directly.

surrounding regions, which are not photoirradiated and are thus FAS-covered, are free of deposits. This clearly indicates that the deposits grown on the UV-irradiated regions stay tightly fix to the surface, while the deposits on the FAS-covered regions have been completely eliminated. On the other hand, no microstructured features can be seen on the micropatterned FAS/PI_{ox} substrate shown in Figure 7b. Both sample surfaces are observed in detail by DFM. As clearly seen in the DFM image in Figure 7c, highly resolved micropatterns composed of tin oxide film grow site-selectively on the photoirradiated regions of the micropatterned FAS/nanolayer/PI_{ox} substrate. In contrast, it is difficult to achieve clear micropatterns on the FAS/PI_{ox} substrate, as shown by Figure 7d. This sample has been treated in absolute toluene for 30 min. As can be clearly seen, the tin oxide remains deposited relatively evenly on the FAS-covered regions and there is marked distortion of the deposits on the UV-irradiated regions. When sonication is prolonged up to 2 h (image not

shown), the micropattern becomes hardly recognizable by DFM. This significant difference in surface morphology between the samples must be considered in terms of the surface chemical properties of the UV-irradiated and the unirradiated regions on both samples. However, since it is difficult to determine the actual surface properties of these regions selectivity, both FAS/nanolayer/PI_{ox} and FAS/PI_{ox} substrates before and after VUV irradiation without micropatterning are characterized.

Figure 8 shows the variation in the ζ-potential with the pH of UV-irradiated FAS/nanolayer/PI_{ox}, (i.e., SML (silica monolayer)/ONS/PI_{ox}) and FAS/PI_{ox}, (i.e., SML/PI_{ox}) substrates (indicated by the open and solid circles, respectively). As a control experiment, an observation of a SiO_2/Si substrate is also performed in the same manner (indicated by the solid triangles). Over the pH range from 3 to 11, the SiO_2/Si surface shows negative ζ-potentials from ca. –22 to –82 mV due to the partial ionization of surface silanol (Si-OH) groups. The isoelectric point (IEP) of this surface is estimated to pH 2.0. It is noteworthy that the ζ-potential vs pH curves for the SML/ONS/PI_{ox} and SiO_2/Si substrates are nearly identical in shape and magnitude over the entire pH range. Thus, it can be concluded that the UV-irradiated FAS/nanolayer/PI_{ox} surface shows chemical properties very similar to the SiO_2/Si substrate, and that the oxide layers (i.e., the SML and nanolayer) has covered the PI substrate almost completely. On the other hand, the UV-irradiated FAS/PI_{ox} surface is found to 15-39% less charged than the SML/nanolayer/PI_{ox} and SiO_2/Si substrates. In addition, the IEP of this sample, observed to be around pH 3.5, is higher than those of the SML/nanolayer/PI_{ox} and SiO_2/Si substrates. This clearly indicates that the SML insufficiently covered the PI_{ox} surface. Since the density of the FAS molecules is considered to have been low, a very small part of the hydrophilic PI_{ox} surface is probably exposed to air. As a result, the molecules at the bottom of the FAS comprising SML are loosely packed. This marked difference in surface properties must account for both the final morphology and the adhesion properties of the deposits on the UV-irradiated regions.

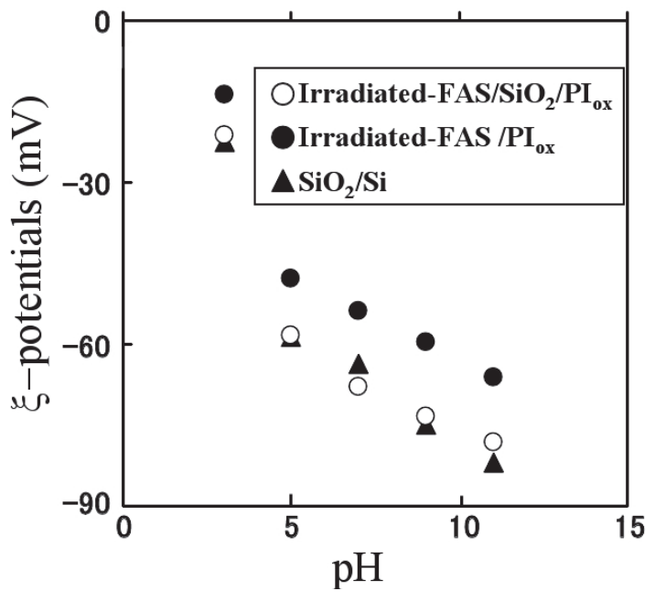

Fig. 8. Comparison of ζ-potentials as a function of pH for an irradiated FAS/nanolayer/PI_{ox} (open circles), an irradiated FAS/PI_{ox} (solid circles), and a silicon covered with native oxide (solid triangles), respectively. SML means siloxane monolayer.

SAM formation technique demonstrated here offers the advantage that, by selecting an organosilane precursor, a well-ordered SAM with a wide variety of terminal-end groups can be fabricated on a mechanically-flexible polymer sheet (not only PI) without any marked change in surface morphology or bulk properties. Thus I expect this technique to be readily and widely applicable to novel polymer surface modification based on organosilane SAM chemistry. In addition, patterned SAM-covered polymer substrates could be applied as microtemplates for the site-selective immobilization of various kinds of materials including biomolecules, semiconductors and other functional molecules to fabricate novel polymer-based flexible devices.

3. Parallel detection of biomolecular recognition event on a microarray of monolayers

Direct-writing using molecular ink plays a leading role in the development of bottom-up nanofabrication, due to its unparalleled, lithography-free properties, that allow precise positioning of the ink on a predefined surface site to obtain a high-resolution pattern on a substrate. To date, a number of direct-writing methods including microcontact printing, dip-pen nanolithography (DPN), microfluidic devices, nanoscale pipetting, and inkjet printing have been developed. A combination with either one of the molecular inks including SAMs, oligonucleotides, proteins, carbohydrates, nanoparticles, and polymers leads to the fabrication of its fine pattern. Many works in SAM chemistry have used the high resolution SAM patterns in particular, as chemical templates that serve as prospective candidates to miniaturize and simplify traditional laboratory techniques, bioassays, cell culture experiments, and multifunctional gas-sensing array. Achieving these goals requires the production of a chemical template in which different varieties of SAMs are precisely positioned on predefined surface sites on a given substrate. Thus far, a SAM system using a combination of thiol-ink and gold-substrate, i.e., ink-paper chemistry, has already satisfied this requirement. Actually, Mirkin and co-workers produced a microarray of four different alkanethiol SAMs by DPN [7]. The chemical functionalization of the gold surface allows the use of surface plasmon resonance and an oxidation-reduction potentiometer to detect the chemical or biomolecular interaction on thiol-template. However, its high-conductivity and optical inflexibility in the visible region has often limited the enviable versatility of SAM microarrays. This section thus describes the novel methodology to produce SAM microarrays on other substrates including glass, oxidized silicon, OH-terminated diamond, metal oxides, and polymers. The transparency in the visible region of glass is particularly essential to study biomolecular interactions under the microscope. Moreover, using a substrate diamond having both transparency and conductivity facilitates the electrochemical detection of specific biomolecular events.

The lithography-free method for oxide-based microarrays starts with the transfer of an alkoxysilane ink to the predefined surface position on an oxidized substrate under ambient conditions, as shown in Figure 9. A wide variety of pens including syringe and AFM tips can be lined up as candidates for painting with molecular inks. To verify the methodological potential, three different types of trialkoxysilanes, that is, triethoxysilylundecanal (TESUD), N-(6-aminohexyl)-3-aminopropyltrimethoxysilane (AHAPS), and octadecyltrimethoxysilane (OTS), are selected as model molecular inks. As shown in Figure 9, these organosilane inks are respectively transferred from the tips of syringes onto the predefined surface positions. At each deposit, silanization occurs during hydrolysis of the alkoxy groups by physisorbed

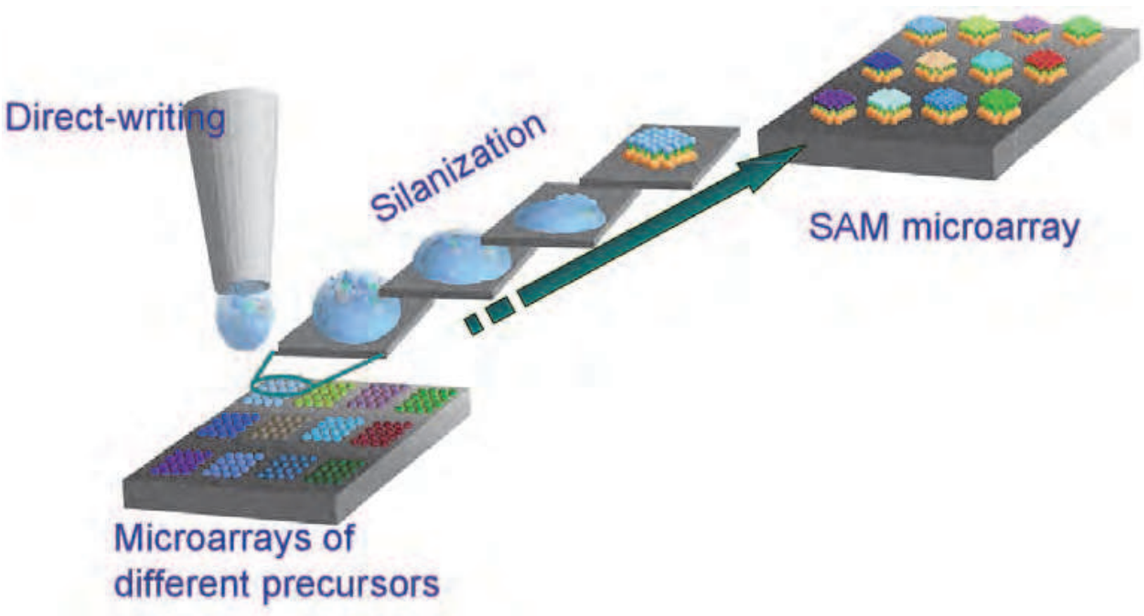

Fig. 9. Schematic illustration showing ink-paper chemistry on oxide substrate to fabricate a siloxane-based SAM microarray.

water on the hydrated surface, followed by a condensation reaction to give an interfacial covalent linkage between the silane molecule atom and the substrate. All of the analyses shown in Table 3 suggest that the alkoxysilane molecules form their one-molecular thick structures by the SAM formation process. The measurement of the water-contact angle is still a facile and useful method for estimating SAM formation. A high value of the water-contact angle for the OTS-treated sample is comparable to that of OTS-SAM prepared by chemical vapor deposition. A correspondence in the surface wetting property is observed between the AHAPS-treated sample and amine-terminated SAMs. The prepared OTS- and AHAPS-treated samples are then analyzed using atomic force microscopy (AFM) and ellipsometry. Although the ellipsometrical thickness of the AHAPS-treated sample is fairly in good agreement with that of AHAPS-SAM structure, the OTS-treated film is slightly thinner than its ideal thickness, that is, 25–28 Å. As expected in the case of small water-contact angle hysteresis $\Delta\theta$, which is defined as $\Delta\theta = \theta_a - \theta_r$, both the samples' surface roughnesses measured by AFM at angstrom level are small, resulting in the successful formation of SAMs with or without less defective surfaces. On the other hand, the water-contact angle of TESUD-treated samples is substantially lower than that of the non-orientated TESUD-SAMs (e.g., $\theta_{a/r}$ = 78.1°/76.2°). In order to elucidate the lower water contact-angles for this TESUD-treated sample, attenuated total reflection Fourier transform infrared (ATR-FTIR) spectroscopy, which is a convenient and well-established method of examining a SAM in surface chemical composition and intermolecular packing structure, is used. The frequencies of antisymmetric and symmetric methylene stretching modes are important indicators for exploring in-plane structures, including molecular ordering of alkane chains. The appearance of the $\nu_a(CH_2)$ at 2925−2930 cm^{-1} and the $\nu_s(CH_2)$ at 2855−2858 cm^{-1} suggests that the hydrocarbon chains in a SAM structure are disordered,

resulting in a liquid alkane or an amorphous film. In contrast, shifts from their vibrational peak positions to the frequencies of $\nu_a(CH_2)$ and $\nu_s(CH_2)$ centered at 2917 cm^{-1} and 2950 cm^{-1} indicate the formation of a highly crystalline ordered SAM structure due to the strong hydrophobic interactions between adjacent alkyl chains. On the basis of this common monomolecular packing theory, the methylene stretching vibrations observed at 2916 cm^{-1} for $\nu_a(CH_2)$ and at 2849 cm^{-1} for $\nu_s(CH_2)$ in the sample, indicate that the internal hydrocarbon chains are completely ordered to produce the solid TESUD-SAM structure. Due to this well-ordering, the TESUD-SAM has a higher hydrophilic surface property, and is slightly thicker than the disordered structures (d_{ellips} = 1.2–1.4 nm). The frequencies of $\nu_a(CH_2)$ and $\nu_s(CH_2)$ for the OTS-SAM are respectively observed at 2922 cm^{-1} and 2852 cm^{-1}, which suggests that this monolayer is relatively ordered when compared with its amorphous film. In Table 3, the ATR-FTIR measurement indicates that the molecular structure of the AHAPS-treated sample is akin to a non-crystalline film, but its molecular thickness and surface wetting properties correspond approximately to the reported values (d_{ellips} = 1.1−1.3 nm, $\theta_{a/r}$ = 62.0±3°/58.0±2°). Due to the limited early reports about AHAPS-SAM, further comparison is restricted, but the measurements shown in Table 1 yield conclusive evidences about the formation of a single-molecule thick structure of AHAPS.

Reactants	Water contact-angle $\theta_{a/r}$ (deg.)	Thickness d_{ellips} (nm)	asymmetric stretch $\nu_a^{p\text{-}pol}$ (cm^{-1})	$\nu_a^{s\text{-}pol}$ (cm^{-1})
OTS $CH_3(CH_2)_{17}Si(OCH_3)_3$	108°/97°	1.96 ± 0.1	2922	2852
TESUD $CHO(CH_2)_{10}Si(OC_2H_5)_3$	69°/62°	1.44 ± 0.1	2916	2849
AHAPS $NH_2(CH_2)_6NH(CH_2)_3Si(OCH_3)_3$	58°/50°	1.29 ± 0.2	2925	2855

Table 3. Surface characterization of OTS-, TESUD-, and AHAPS-treated films.

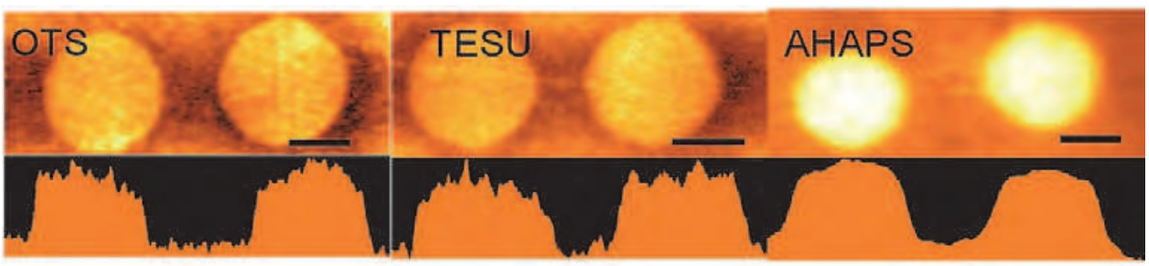

Fig. 10. KPFM and cross-sectional images of the microstructured OTS-, TESU-, and AHAPS-SAMs formed on SiO_2/Si substrate

As shown in Figure 10, SAMs' structures shown in Table 3 are microfabricated, and are analyzed using Kelvin probe force microscopy (KPFM), which promotes a better understanding of the difference in chemical properties between the SAM−covered and −uncovered surfaces. As expected, the coplanar microstructures of OTS/SiO_2, TESUD/SiO_2, and AHAPS/SiO_2 are clearly imaged through the difference in surface potential between the

SAM-covered and -uncovered regions, respectively. In the images, the round-shaped features, as well as their frictional contrast images are highly resolved. Besides, the surface potential of the surrounding SiO_2 surfaces is consistently lower in magnitude than those of every SAM-covered region. Depth distribution profiles acquired from those KPFM images show potential difference between the SAM-modified and -unmodified surfaces of about 6 mV (for TESUD/SiO_2), 18 mV (for ODS/SiO_2) and 37 mV (for AHAPS/SiO_2), respectively. A surface potential distribution between the SAM-covered and –uncovered regions is given by following equation [8-10]:

$$\Delta V_{SAM\text{-}SiOH} = \mu / A\varepsilon_{SAM}\varepsilon_0$$

where μ is the actual molecular-dipole moment normal to the substrate, ε_{SAM} and ε_0 are the permittivity of the SAM and the free space, respectively, and A is the area occupied by the molecule. Accordingly, a comparison of the theoretical dipole moment between two different surfaces leads to the identification of the terminal functional-group of the SAM, in addition to its molecular packing density. In order to calculate the dipole moments of the SAMs' precursors used here, their simplified molecular models are assumed, as shown in Figure 11. In the model SAMs, the molecules lie perpendicular to the substrate, and the terminal silicon atoms in their head-groups are replaced with hydrogen atoms. Since the directional vector of a dipole moment points from the positive charge source to the negative charge source, the three types of SAM-covered surfaces shown in KPFM images must have a positive potential contrast when compared with the surrounding SiO_2 surface. In Figure 11, the theoretical dipole moment of the AHAPS-model is 29.91 Debye, oriented to the substrate with a 0° of tilt angle to its alkyl chain. The amorphous-like molecular structure of AHAPS-SAM does not allow the estimation of its tilt-angle by ATR-FTIR, but the direction of its theoretical dipole moment is consistently toward the substrate, regardless of the actual molecular tilt angle. The dipole moment of the OTS-model is equal to 0.85 Debye, and is tilted at 150.0° from the surface normal. This indicates that the OTS-SAM has a positive surface potential higher than the surrounding SiO_2 surface. On the other hand, the dipole moment of the TESUD-model is tilted at 90° to the surface normal. The component of its dipole moment vertical to the substrate is thus almost zero. In order to explain the surface potential in contrast to TESUD/SiO_2, the most probable dipole moment is determined as follows. Prior to the calculation of the molecular dipole moment, ATR-FTIR is used to estimate the tilt angle of the TESUD-SAM by measuring its dichroic ratio, given the strong dependence between the molecular orientation and the direction of dipole moment. The dichroic ratio, which is defined as the ratio of peak-intensity of the s-polarized absorbance, A^{s-pol}, to p-polarized absorbance, A^{p-pol}, gives information on the molecular tilt angle of a SAM. The dichroic ratio of the asymmetric methylene stretch observed in the TESUD-SAM has a value of 1.05, which is in fairly good agreement with those of the ordered OTS-SAMs prepared by Sagiv (D = 1.03 and 1.09) and Ulman (D = 1.04) [11,12]. Using the IR dichroism data, a tilt angle, θ_{tilt}, is estimated to be 27°, with respect to the surface normal. When the TESUD-SAM is tilted at 27° with respect to the surface normal, the vertical component of the dipole moment is equal to 1.05 Debye oriented towards the substrate. As a result, the positively-charged surface potential of the TESUS-SAM on the SiO_2 matrix is verified. These KPFM observations indicate that the microscale features of SAM surfaces shows chemical properties very similar to OTS-, TESUD-, and AHAPS-SAMs, respectively.

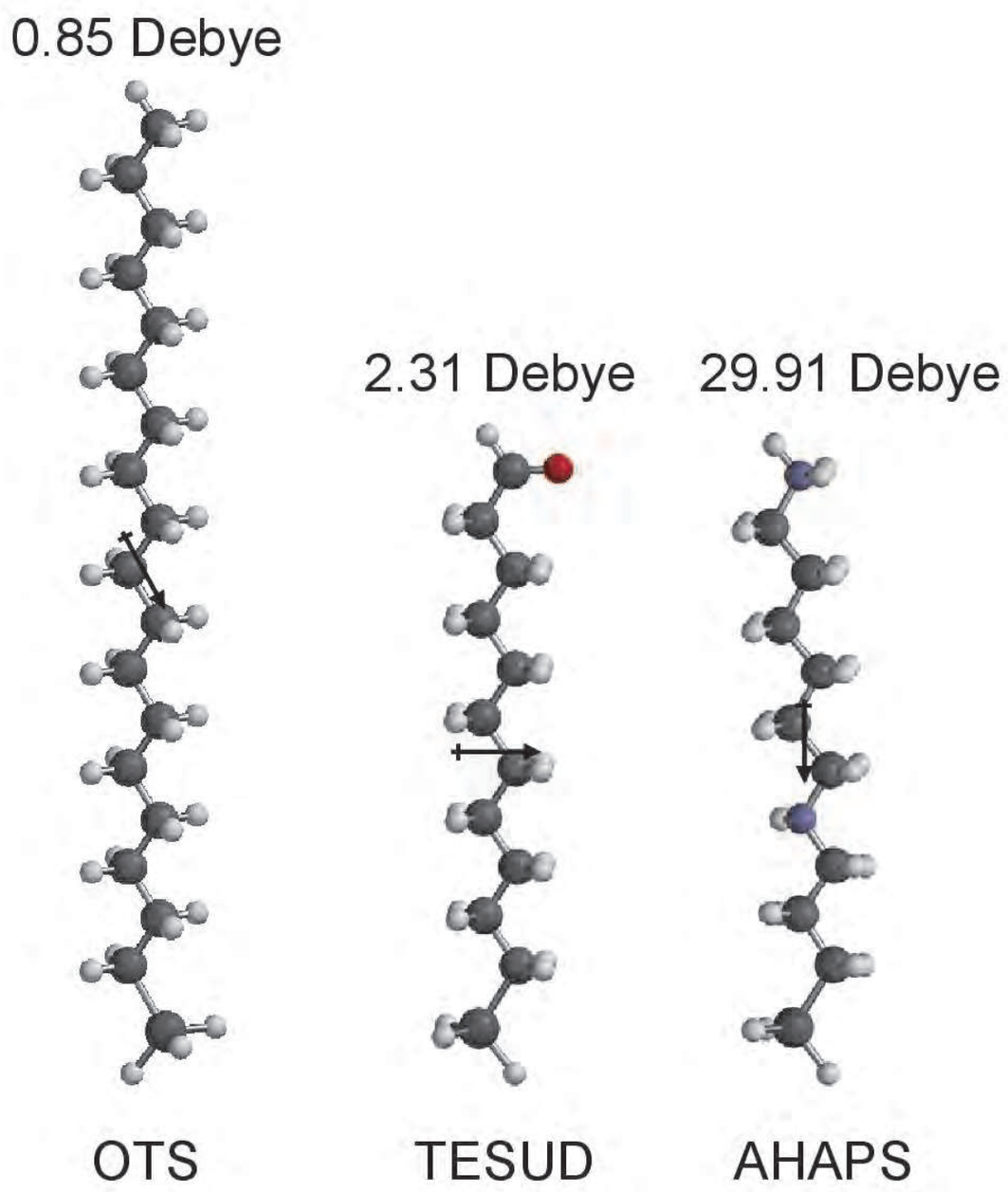

Fig. 11. Molecular structures and dipole moments of the model molecules for OTS, TESUD, and AHAPS-SAMs.

A SAM microarray is produced by combining the non-lithographical method and two different alkoxysilane inks. In a manner similar to that shown in Figure 9, two different molecular inks, TESUD and AHAPS, are respectively positioned under ambient conditions to create a microarray of two silane inks, as shown in Figure 12a. This sample is then treated in a manner very similar to the above-mentioned SAM formation process. Figure 12b shows a KPFM image of the resultant sample. In this surface potential image, well-defined microstructures composed of round-shaped 20 μm features are observed in contrast to the SiO_2 matrix. The surface potential contrasts between SAM-covered and –uncovered regions are +6 mV for TESUD/SiO_2 and +38 mV for AHAPS/SiO_2, respectively. The magnitude of each surface potential contrast approximately corresponds to the values observed in the single microarrays of TESUD- and AHAPS-SAMs in Figure 10. As a result, the successful fabrication of the SAM microarray, in which two different types of SAMs are positioned on each predefined surface site, is confirmed. Next, the potentiality of this SAM microarray as single-molecule thick platform for protein array is examined using protein G, which is an immunoglobulin-binding protein. An amine in protein G reacts with the outermost aldehyde group of the TESUD region on the microarray to give corresponding schiff base, which is reduced to the secondary amine by sodium cyanoborohydride. Throughout this reaction, protein G is covalently immobilized onto the TESUD-SAM surface. Due to the use of protein primarily labeled with Alexa 488, its presence on the sample surface is observed under a fluorescence microscope. As shown in Figure 12c, a strong fluorescence signal is detected with area-selectively on the TESUD-covered region. This successful detection, even after strong surface-cleaning, implies that protein G is not simply physisorbed, but is covalently bound to the aldehyde-terminated SAM surface. In contrast, the dark areas in Figure 12c correspond to the regions covered with AHAPS-SAM. This indicates that the AHAPS-SAM surface strongly prevents even nonspecific adsorption of protein G from the contacting buffer when compared with that on SiO_2 matrix. Accordingly, the fluorescence signal from the Alexa-labeled protein is the highest in magnitude on the TESUD-SAM region of the microarray.

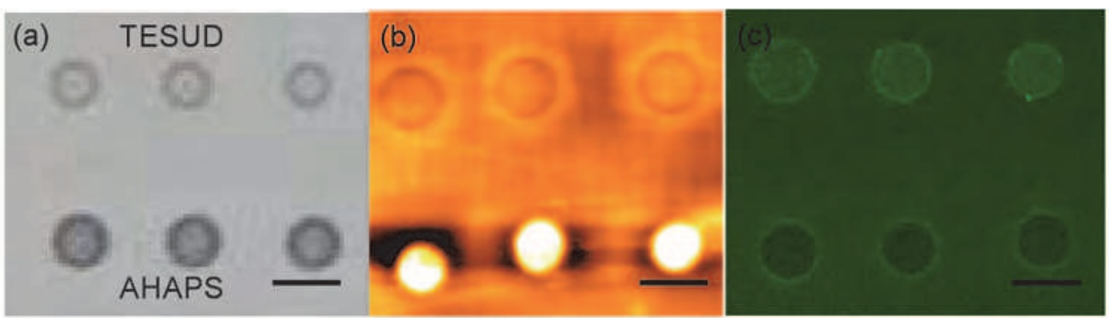

Fig. 12. (a) Optical image of a microarray having droplets of AHAPS and TESUD molecules, (b) KPFM image of TESUD/AHAPS-SAMs microarray, (c) Fluorescence microscopic image of TESUD/AHAPS-SAMs microarray after treated with Alexa-labeled Protein G. Scale bar: 20 μm.

As demonstrated here, the use of SAM microarray allows the parallel detection of different protein-behaviors on one platform surface under same experimental conditions. Although the two different kinds of SAMs are microstructured in this case, further increase in varieties

will allows the parallel detection of many host-guest molecular interactions. Thus, such parallel observation of different variations in chemical reaction and biomolecular interaction on the same platform, where a number of different functional SAMs are integrated at predefined positions, will be able to lead to the achievement of facile and fast medical screening, or miniaturizations of traditional laboratory techniques, bioassays, and cell culture experiments.

4. Highly luminescent silicon nanoparticles

4.1 Background

Si is one of the most common chemical elements; it can be found everywhere and makes up 28% of Earth's crust by mass. Bulk Si wafers, which provide a platform for large-scale integrated circuits in modern microelectronics, are essential in consumer electronics, but have not attracted interest in the fields of optics and optoelectronics. This is because of its indirect bandgap nature due to which the minimal-energy state in the conduction band differs in a k-vector of the Brillouin zone from the maximal-energy state in the valence band. Therefore, in 1990, the discovery of red light emission from porous Si with a quantum yield (QY) of 1%, which was 10,000 times higher than that of bulk Si, created a sensation. As a result, many researchers recognized other features of Si that are useful in functional applications, including illumination sources. Free-standing nanoparticles provide much higher QYs than do porous Si. The emission color can be tuned in an astonishingly wide range from near-UV through visible to near-IR wavelengths, but the direct relationship between size and optical properties is still poorly understood, and thus inhibiting reproducible synthesis of luminescent Si nanoparticles with distinct emission spectra. In this section, I provide a brief overview of recent progress in this field, and highlight some of the most pertinent parameters to improve luminescence quality from Si nanoparticles. To achieve the color tunability, interfacial configuration formed between monolayers and nanoparticles is one of keys [14]. The difference in the interfacial chemical property affects on the optical absorption and emission properties of Si nanoparticles. Perhaps, the most obvious model for this demonstration is a colloidal form of nanoparticles. Furthermore, a high chemical affinity of Si has the potential to produce unlimited variations in the derivatives of the nanoparticles that can be mounted on optical and optoelectronic applications.

4.2 Synthesis of Si nanoparticles

A hydrogen-terminated silicon surface, which is habitually used as in semiconductor processing, is used as a basal plane in a chemical modification, as demonstrated in this study. Many methods have been developed for H-terminated silicon nanocrystal synthesis, as listed in Table 4. Among these methods, the most widely used ones are the mechanical fracturing of H-terminated silicon wafers and the gas-phase decomposition of silane or organosilane gas. Mechanical fracturing is further classified into two types: electrochemical anodization and pulsed laser ablation. Electrochemical etching, which is a well-known method for porous silicon production, is normally performed by anodic oxidation of H-terminated silicon wafers with a mixture of hydrofluoric acid (HF) and hydrogen peroxide. Therefore, nanocrystals can be obtained from the anodically etched wafer, i.e. porous silicon. Although their size distributions are broad, a relatively large quantity of luminescent

Methods	References
Electrochemical anodization	15—19
Pulsed laser ablation	20—23
Gas-phase decomposition	24—30
Liquid phase solution synthesis	31—33

Table 4. A list of representative methods for the preparation of silicon nanoparticles

crystals can be produced. On the other hand, pulsed laser ablation, generates extremely narrow size distribution of silicon nanocrystals. In a typical experimental setting, an H-terminated wafer of silicon is placed on a rotating target holder in a vacuum chamber, and then is ablated at the focal point of a laser beam. The ablation generates large quantities of vapors of elemental silicon. The vapors then assemble to form nanostructured configurations, such as nanoparticles and/or nanoparticles. The successful preparation of such nanosized configurations requires careful control in the experimental process. A wide variety of lasers, such as YAG, CO_2, N_2, KrF and ArF, have been hitherto employed for the ablation. An inert gas such as helium, introduced into the chamber, prevents unfavourable reactions with small amounts of oxygen that exists even in vacuum conditions. The background gas pressure influences the particle size distribution. In addition, the laser irradiation density affects the particle sizes and their distribution. The laser ablation method utilizes the homogeneous vaporization and subsequent rapid condensation to achieve high monodispersity. Generally speaking the drawback of the use of laser ablation method is lower yield of the nanoparticles. Since the early investigation by Brus [24], the gas-phase decomposition of silane or organosilane molecules has been studied. In general, such silane-based gases together with helium and hydrogen are introduced into the reaction field within the vacuum chamber, and are pyrolytically decomposed at high temperature, typically 950^{o}C, which results in a silicon nanoparticle. In addition to CO_2 lasers, microwave plasmas are also effective for similar thermal decomposition. Both methods, i.e., mechanical fracturing and gas-phase decomposition, are technically practicable for producing large amounts of silicon nanoparticles; however, subsequent chemical etching caused by the acidic system, composed of HNO_3/HF or HF, is definitely required for the complete passivation of outermost silicon layer with hydrogen atom. The first report about successful liquid phase solution synthesis was achieved by Hearth [31]. Since then, several methods for producing H-terminated silicon nanoparticles have been reported, as listed in Table 1. Hydrogen reduction of silicon halides, i.e. SiX_4 where X = Cl, Br or I, by metal hydrides such as lithium aluminium hydride ($LiAlH_4$, LAH) is the most common synthesis route. Moreover, the reductive reaction is basically performed in a non-polar aliphatic solvent with complete absence of oxygen and water molecules in an inert atmosphere. The LAH reduces Si(IV) to Si(0). Next, the neutral Si(0) assembles to form nanoparticles with a passivation layer of Si-H (318–351 kJ/mol), as schematically illustrated in Figure 13. In the hydride reduction process, the additional use of an inverse micelle such as tetraoctylammonium bromide leads to remarkable improvement in size monodispersity because the nanoscale gauge formed by the inverse micelle controls the final crystal size. Unlike mechanical

fracturing and gas-phase decomposition, hydride reduction enables complete passivation of the crystalline surface. Therefore, this method does not require subsequent HF treatment. The use of a metal silicide promises large quantity synthesis of silicon nanoparticles even by a liquid phase solution process. For example, Kauzlarich and co-workers successfully produced more than a decamilligram of silicon nanoparticles by the following chemical reaction [33]:

$$NaSi + NH_4Br \rightarrow Si/H + NaBr + NH_3 \quad (1)$$

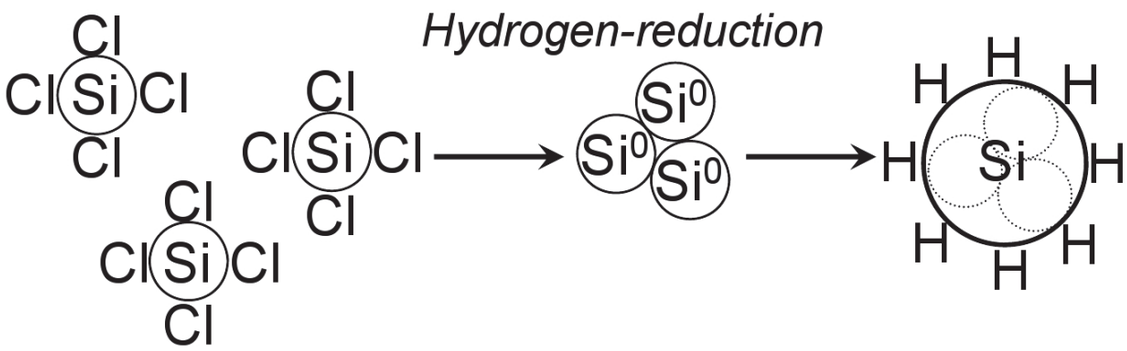

Fig. 13. Hydrogen reduction process for H-terminated silicon nanoparticles.

Identification of the chemical bonding states of a nanoparticle's surface has been frequently performed by Fourier transform infrared spectroscopy (FT-IR). Absorption at around 2100 cm^{-1} indicates the presence of the Si-H_x stretch. On the other hand, the relatively broad peak observed at 1000–1100 cm^{-1} can be attributed to the Si-O-Si linkage, which indicates that the silicon surface is oxidised. More than 99% of the outermost silicon atoms can be hydrogen terminated; however, complete absence of oxygen is a difficult-to-achieve goal on a nanoparticle. As a clear-cut example, some samples were prepared by laser pyrolysis of gaseous silane, and then were etched with a mixture of HF (48 wt%) and HNO_3 (69 wt%). In a FT-IR spectrum of the sample, strong peaks were visible at around 1087 cm^{-1} and 2105 cm^{-1}. In contrast, acidic treatment with HF/HNO_3 (10/1, v/v) was expected to result in non-oxidised surfaces. However, the presence of oxygen, i.e. Si-O-Si, was seen in FT-IR spectrum, although its intensity in absorbance was relatively weak when compared with the first model sample. Therefore, the etching chemistry on a nanoparticle is considerably different from that on a wafer. In fact, the etching rate of native oxide on a wafer is thousands times larger than that of oxidized nanoparticle.

In current microelectronics, halide-terminated surfaces are less used when compared to H-terminated ones; however, they are extremely useful as the starting stages in wet chemistry on silicon nanoparticles. Due to their relatively high reactivity, it is imperative to treat the halogenated surfaces in an inert condition. Following the first demonstration by Heath [31], a series of solution syntheses that use the combination of Zintl salts (KSi, NaSi and Mg_2Si) and $SiCl_4$ have been developed by Kauzlarich and co-workers. In the case of KSi, Si nanoparticles can be obtained through the following reaction:

$$4n\text{KSi} + n\text{SiCl}_4 \rightarrow \text{Si nanoparticle} + 4n\text{KCl} \quad (2)$$

The synthesis utilising Zintl salts presumably produces a chloride-terminated silicon surface, which is very sensitive to oxygen and moisture. For the evaluation of the intra-particle structure FT-IR, solid-state Nuclear Magnetic Resonance (NMR) and High-Resolution Transmission Electron Microscopy (HR-TEM) has been used. A combination of HR-TEM and selected-area diffraction (SAD) has showed the presence of crystalline silicon in a product synthesized by the reaction of Zintl salts with $SiCl_4$; however, macroscopic observation based on ^{29}Si MAS-NMR revealed that the product was composed of a mixture of crystalline and amorphous phases. Unlike X-ray powder diffraction, NMR allows acquisition of structural information even from a small quantity of fluid specimen. In many cases, the Zintl salts are generally synthesized via the reaction of explosively reactive alkali metals with silicon at high temperatures of more than 600°C. Recent technical advancements in wet chemistry have achieved room temperature solution synthesis of Cl-capped silicon nanoparticles using alkali naphthalides as reducing agents. The synthesis of alkali naphthalides is very simple. In particular, alkali naphthalides can be easily prepared at room temperature by the reaction of alkali metals, such as lithium or sodium, with naphthalide. As this reaction requires a moisture-free environment, the use of a dehydrated solvent, such as THF, glyme or diglyme, is necessary. If the reaction is correctly processed, the resultant solution turns dark green in colour. Unlike the reductant sodium naphthalide, it was reported that lithium naphthalide gives only amorphous nanoparticle.

Bromine-terminated silicon nanoparticles can be synthesised by the oxidation of magnesium silicide with bromine, according to the following equation.

$$n\text{Mg}_2\text{Si} + 2.5n\text{Br}_2 \rightarrow \text{Si}_n\text{Br} + 2n\text{MgBr}_2 \quad (3)$$

The reaction with Br_2 requires careful selection of the solvents. Molecular bromine is a strong oxidant capable to decompose ether solvents such as glyme. One possible solution is the use of inert solvents, such as alkanes, for bromine. A halogenated surface shows high reactivity to various functional molecules, such as alcohol, amine, aldehyde, alkyllithium and Grignard reagents, as demonstrated in the following sections.

Structural analysis is performed by combining HR-TEM and either one of XRD, XPS and Raman spectroscopy. It has been widely recognized that the energy position of Si2p spectrum in XPS profile is far from the known position for Si-Si bond, i.e., 99.5 eV because of the presence of charge trapping which arises from monolayer-shells covering NCs. Raman spectrum, which is a powerful macroscopic observation tool, is sensitive to the size and crystallinity of nanoparticles. The relationship between size and Raman peak maxima is summarized in Figure 14. Raman spectrum for crystalline bulk Si exhibits a single distinct peak at 520 cm^{-1} whereas that of amorphous Si is composed of a broad peak at around 476-480 cm^{-1}. Interestingly, a blueshift in the Raman spectrum appears with decreasing physical size, as shown in Figure 14. In particular, a relatively broad Raman peak appears at about 503 cm^{-1}, whereas vibrational features are absent in the 510–517 cm^{-1} region and at around 476 cm^{-1}, suggesting that the majority of the product is constructed of crystalline structures ≤2.5 nm [35]. This was consistent with HR-TEM study [35]. Raman spectroscopy is one of powerful tools to perform macroscopic observation, while microscopic observation requires HR-TEM. According to the careful observation with HR-TEM, a true atomic arrangement is

revealed, as shown in Figure 15. These nanoparticles were prepared at room temperature by sodium biphenylide reduction of $SiCl_4$ in the presence of surfactant, i.e., dimethyldioctyl ammonium bromide (DMDOAB) [35]. In every high-resolution image, periodic arrangements of channel structures surrounded by Si tetrahedrons are clearly visible. The nanoparticles having diameter d > 1.5 nm have diamond cubic lattice structures. The same is true for 1.5-nm nanoparticles; thus, a 1.5-nm nanoparticle is large enough to form a diamond cubic lattice. Interestingly, a 1.1-nm nanoparticle, unlike other nanoparticles, cannot have a diamond cubic lattice. At 1.1 nm, about 30 atoms are required to produce a diamond cubic lattice. Although a complementary simulation study is needed to determine the real atomic geometry, the minimum size that allows the formation of a diamond cubic lattice may be found to lie in the 1.2–1.5-nm size regime.

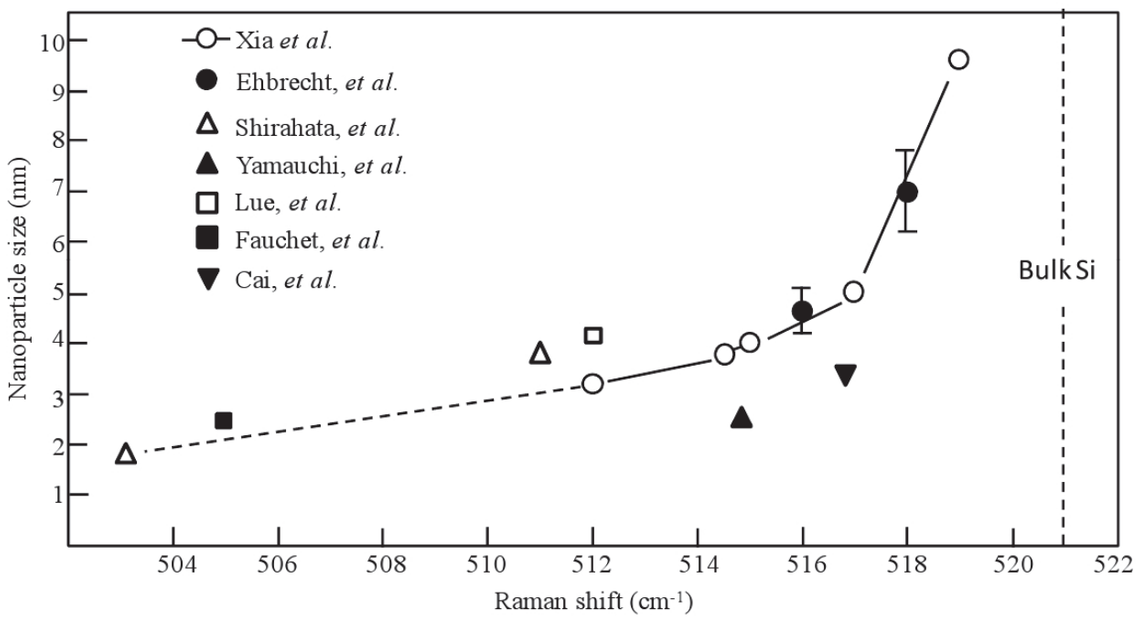

Fig. 14. Comparison of our results with the Raman resonances published by others (refs. 34-41).

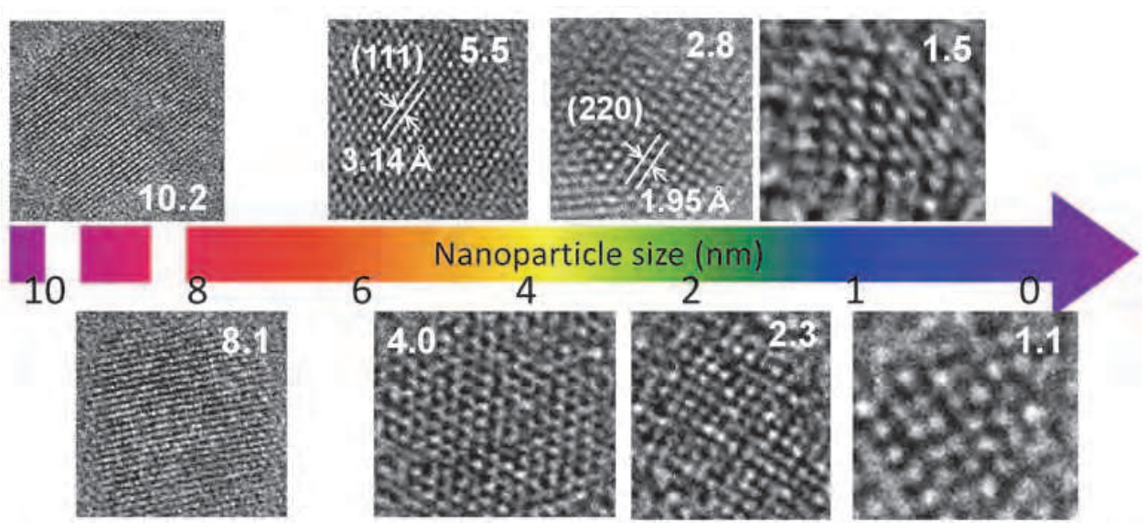

Fig. 15. HR-TEM images showing lattice fringes of the different size of Si nanoparticles synthesized by inverse micelle method [35].

4.3 Surface modification of nanoparticles

An elemental Si exhibits a high chemical affinity for carbon, oxygen, nitrogen and sulfur. The first three elements form covalent bonds with Si and provide the differences in polarity. On the other hand, sulfar can interact specifically with Si as well as gold, yielding a S-Si linkage. Such a range of options in mode of binding creates variations in the organic derivatives of Si nanoparticles hybridized at the molecular level. As shown in Figure 16, various chemical routes are available for modifying the surface of Si nanoparticles as in to the case with wafer chemistry [14,43]. Interestingly, a molecular attachment to the surface of nanoparticles yields the change in physical nature from solid products to viscous liquid, because the organics possibly dominate the physical nature in such nanoparticle systems [42]. Therefore, surface modified nanoparticles are easily soluble in any solvents without severe sonication. The most comprehensive and accessible are the use of luminescent nanoparticles as fluorophors for biomolecular imaging and monitoring. To give water-solubility, the end groups of monolayer-capped nanoparticles are modified into either one of hydrophilic groups including amine, carboxyl, aldehyde, ester, oligonucleotides, and carbohydrate [14]. As shown in Figure 16a, water-soluble luminescent Si nanoparticles exhibit the superior stability against photobleaching when compared to conventional organic dyes. Furthermore, the presence of surface monolayers gives nanoparticles an exceptional stability over a wide pH range (pH=1-13) and high temperatures (120°C), and influences on a cytotoxicity of NCs [44,45]. Therefore, their use allows the prolonged monitoring of specific biomolecular interaction events and a parallel detection of different molecular recognitions. A recent investigation for bioimaging is demonstrated in Figure 16b [46]. In this fluorescence observation, a two-photon microscopic image of microphage cell when excited with a 780 nm of laser is presented. As clearly seen in inter-comparison experiment of (c) and (d), the presence of the luminescent nanoparticles in the cytoplasm of the incubated cell is visible, indicating the endocytic mode of internalization. In order

to avoid the photodamage, the use of low photon energy as an excitation source is suitable for applications in dense tissue imaging. These fluorescence images verify the successful in-vitro imaging using a multiphoton microscopy. Thus, organic derivatives of Si nanoparticles have a great potential to be used in a wide variety of optical and optoelectronic applications.

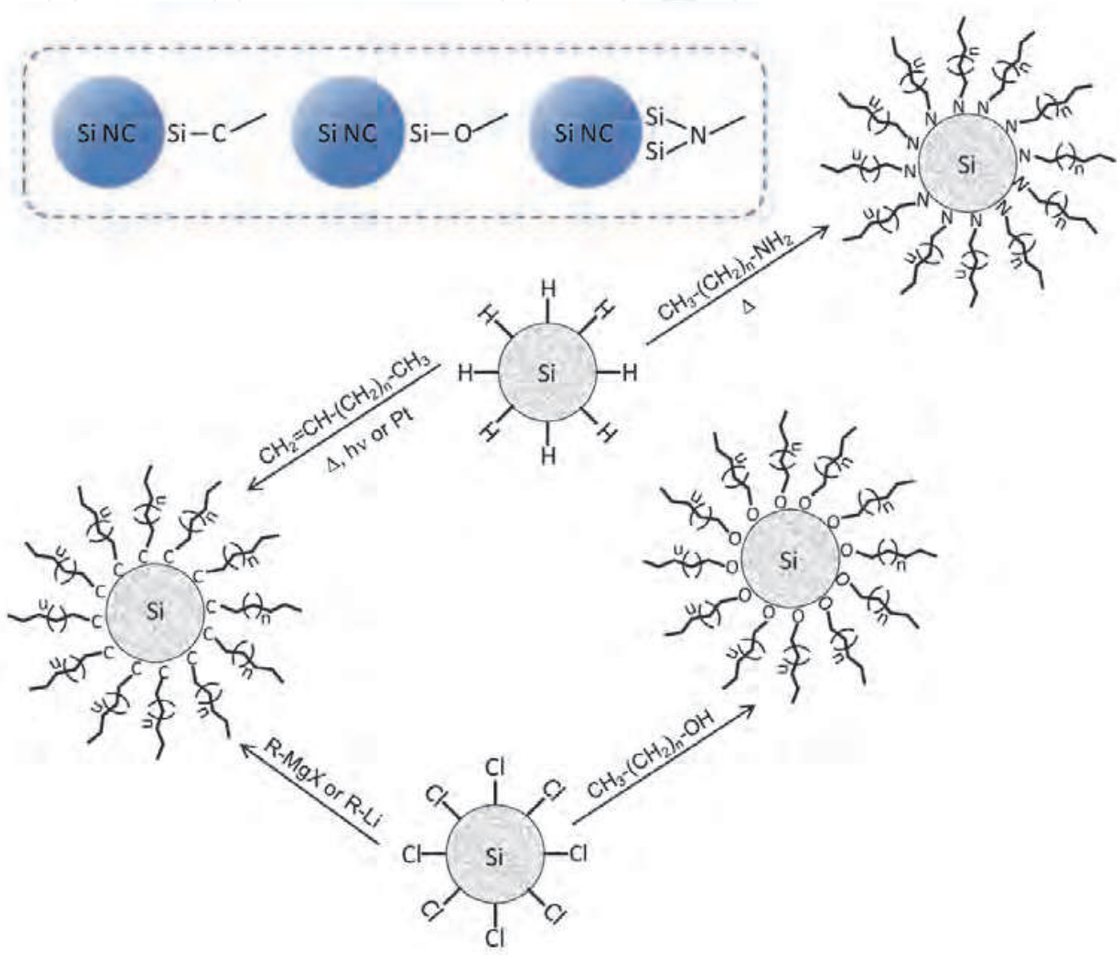

Fig. 16. Representative modification routes for monolayer attachment to the surfaces of hydrogen- and chloride-terminated silicon nanoparticles.

5. Summary

In this article, some of programmed surfaces are demonstrated as models using organic monolayers. Organic films including self-assembled monolayers, which works as a prototypical chemical template and linkers, plays an important role in the development of bioinspired inorganic materials. Due to SAMs' high ability to assemble onto the surfaces of any geometry, size, and component, their employments allow a general and highly flexible

industrial uses. SAMs enable the control of various surface functions including wettability, electrochemistry, magnetism, friction, biofunctionality, and others. The notable advance of top-down lithography approach will be able to produce fine structures in tens of nanoscale resolution, but real nanostructures (or parts) must require to be produced by self-assembly processing. Silicon is one of the few nontoxic, abundant, and environmentally friendly elements, and it has dominated the microelectronics industry owing to its impressive performance as an electronic material. Therefore, the optical use of Si could rapidly gain popularity for its ability to help build a sustainable society by turning indirect bandgap semiconductors like Si and Ge into efficient light emitters. Another great attraction of luminescent Si is the potential ability to tune the emission photon energy over a very wide range from 1.1 eV (for bulk) to 4.0 eV, if high efficiencies of light emissions at each wavelength in the ranging from near-IR to near-UV region are achieved. Furthermore, Si exhibits high chemical affinity for covalent linkages with carbon, oxygen, and nitrogen, which can produce a variety of organic derivatives hybridized at the molecular level. A well-designed ligand working as a molecular wire is expected to decrease a potential energy barrier between nanoparticles and monolayers, leading to the efficient electronic conduction. In addition to the use as fluorescent material for molecular labeling, the chemical compatibility could generate further vitality in its optical use even for fragile items which have direct contact with our skin, such as textile fabrics, cosmetics and paints. Rigorous control of size distribution, surface/interface chemistry and structural phase of Si nanoparticles provides a readily accessible range of color with high purity, and direct grafting of molecular chains on the nanoparticles creates unlimited variations in sophisticated architectures in which Si islands are positioned in a molecular networking matrix.

6. References

[1] N. Shirahata, W. Shin, N. Murayama, A. Hozumi, Y. Yokogawa, T. Kameyama, Y. Masuda K. Koumoto, Adv. Funct. Mater. 14 (2004) 580.
[2] N. Shirahata, W. S. Seo, T. Kinoshita, T. Yonezawa, A. Hozumi, Y. Yokogawa, T. Kameyama, Y. Masuda, K. Koumoto, Langmuir 20 (2004) 8942.
[3] A. Hozumi, M. Inagaki, N. Shirahata, Surf. Sci. 600 (2006) 4044.
[4] Y. Yamanoi, N. Shirahata, T. Yonezawa, N. Terasaki, N. Yamamoto, Y. Matsui, K. Nishio, H. Masuda, Y. Ikuhara, H. Nishihara, Chem. Eur. J. 12 (2005) 314.
[5] N. Shirahata, A. Hozumi, Chem. Mater. 17 (2005) 20.
[6] A. Hozumi, S. Asakura, A. Fuwa, N. Shirahata, T. Kameyama, Langmuir 21 (2005) 8234.
[7] A. Ivanisevic, K. V. McCumber, C. A. Mirkin, J. Am. Chem. Soc. 124 (2002) 11997.
[8] V. Palermo, M. Palma, P. Samorì, Adv. Mater. 18 (2006) 145.
[9] A. Liscio, V. Palermo, D. Gentilini, F. Nolde, K. Müllen, P. Samorì, Adv. Funct. Mater. 16 (2006) 1407.
[10] K. Hayashi, N. Saito, H. Sugimura, P. Takai, N. Nakagiri, Ultramicroscopy 91 (2002) 151.
[11] N. Tillman, A. Ulman, J. S. Schidkraut, T. L. Penner, J. Am. Chem. Soc. 110 (1998) 6136.
[12] R. Maoz, J. Sagiv, J. Colloid Interf. Sci. 100 (1984) 465.

[13] N. Shirahata, J. Nakanishi, Y. Echikawa, A. Hozumi, Y. Masuda, S. Ito, Y. Sakka, Adv. Funct, Mater. 18 (2008) 3049.
[14] N. Shirahata, Phys. Chem. Chem. Phys. (Perspective Article) 13 (2011) 7284.
[15] J. L. Heinrich, C. L. Curtis, G. M. Credo, M. J. Sailor, K. L. Kavanagh, Science 255 (1992) 66.
[16] R. A. Bley, S. M. Kauzlarich, J. E. Davis, H. W. H. Lee, Chem. Mater. 8 (1996) 1881.
[17] M. H. Nayfeh, N. Barry, J. Therrien, O. Akcakir, E. Gratton, G. Belomoin, Appl. Phys. Lett. 78 (2001) 1131.
[18] L. Wang, V. Reipa and J. Blasic, Bioconjugate Chem. 15 (2004) 409.
[19] J. Choi, N. S. Wang and V. Reipa, Langmuir 23 (2007) 3388 .
[20] T. Seto, Y. Kawakami, N. Suzuki, M. Hirasawa and N. Aya, Nano Lett. 1 (2001) 315.
[21] E. Werwa, A. A. Seraphin, L. A. Chiu, Chuxin Zhou and K. D. Kolenbrander, Appl. Phys. Lett. 64 (1994) 1821.
[22] T. Makimura, Y. Kunii and K. Murakami, Jpn. J. Appl. Phys. 35 (1996) 4780.
[23] L. Patrone, D. Nelson, V. I. Safarov, M. Sentis, W. Marine and S. Giorgio, Appl. Phys. Lett. 87 (2000) 3829.
[24] W. L. Wilson, P. J. Szajowski and L. E. Brus, Science 262 (1993) 1242.
[25] M. L. Ostraat, J. W. De Baluwe, M. L. Green, L. D. Bell, M. L. Brongersma, J. Casperson, R. C. Flagan and H. A. Atwater, Appl. Phys. Lett. 79 (2001) 433.
[26] L. E. Brus, P. J. Szajowski, W. L. Wilson, T. D. Harris, S. Schuppler, P. H. Citrin, J. Am. Chem. Soc. 117 (1995) 2915.
[27] G. Ledoux, J. Gong and F. Huisken, Appl. Phys. Lett. 79 (2001) 4028.
[28] X. Li, Y. He, S. S. Talukdar and M. T. Swihart, Langmuir 19 (2003) 8490.
[29] F. Hua, F. Erogbogbo, M. T. Swihart and E. Ruckenstein, Langmuir 22 (2006) 4363.
[30] H. Takagi, H. Ogawa, Y. Yamazaki, A. Ishizaki, T. Nakagiri, Appl. Phys. Lett. 56 (1990) 2379.
[31] J. R. Heath, Science 258 (1992) 1131.
[32] J. P. Wilcoxon and G. A. Samara, Appl. Phys. Lett. 74 (1999) 3164.
[33] D. Neiner, H. W. Chiu and S. M. Kauzlarich, J. Am. Chem. Soc. 128 (2006) 11016.
[34] N. Shirahata, M. R. Linford, S. Furumi, L. Pei, Y. Sakka, R. J. Gates and M. C. Asplund, Chem. Commun. (2009) 4684.
[35] N. Shirahata, T. Tsuruoka, T. Hasegawa and Y. Sakka, Small 6 (2010) 915.
[36] H. Xia, Y. L. He, L. C. Wang, W. Zhang, X. N. Liu, X. K. Zhang, D. Feng and H. E. Jackson, Appl. Phys. Lett. 78 (1995) 6705.
[37] M. Ehbrecht, B. Kohn, F. Huisken, M. A. Laguna and V. Paillard, PRB 1997, 56, 6958
[38] P. Shen, N. Uesawa, S. Inasawa, Y. Yamaguchi, JMC 2010, 20, 1669
[39] S. –K. Ma and J. T. Lue, Thin Solid Films 1997, 304, 353.
[40] J. von Behren, et al., Solid State Commun. 1998, 105, 317.
[41] W. Cai, et al., JAP 2008, 104, 023516
[42] N. Shirahata, S. Furumi and Y. Sakka, 311 J. Cryst. Growth (2009) 634.
[43] N. Shirahata, A. Hozumi, T. Yoenzawa, Chem. Rec. 5 (2005) 145.
[44] M. Rosso-Vasic, E. Spruijt, Z. Popović, K. Overgaag, B. Van Lagen, B. Grandidier, D. Vanmaekelbergh, D. Domínguez-Gutiérrez, L. De Cola and H. Zuilhof, J. Mater. Chem. 19 (2009) 5926.

[45] L. Ruizendaal, S. Bhattacharjee, K. Ournazari, M. Rosso-Vasic, L. H. J. De Haan, G. M. Alink, A. T. M. Marcelis and H. Zuilhof, Nanotoxicology 3 (2009) 339.
[46] C. Tu, X. Ma, P. Pantazis, S. M. Kauzlarich and A. Y. Louie, J. Am. Chem. Soc. 132 (2010) 2016.

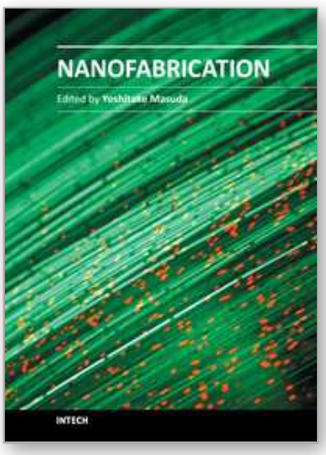

Nanofabrication

Edited by Dr. Yoshitake Masuda

ISBN 978-953-307-912-7
Hard cover, 354 pages
Publisher InTech
Published online 22, December, 2011
Published in print edition December, 2011

We face many challenges in the 21st century, such as sustainably meeting the world's growing demand for energy and consumer goods. I believe that new developments in science and technology will help solve many of these problems. Nanofabrication is one of the keys to the development of novel materials, devices and systems. Precise control of nanomaterials, nanostructures, nanodevices and their performances is essential for future innovations in technology. The book "Nanofabrication" provides the latest research developments in nanofabrication of organic and inorganic materials, biomaterials and hybrid materials. I hope that "Nanofabrication" will contribute to creating a brighter future for the next generation.

INTECH
open science | open minds

InTech Europe
University Campus STeP Ri
Slavka Krautzeka 83/A
51000 Rijeka, Croatia
Phone: +385 (51) 770 447
Fax: +385 (51) 686 166
www.intechopen.com

InTech China
Unit 405, Office Block, Hotel Equatorial Shanghai
No.65, Yan An Road (West), Shanghai, 200040, China
中国上海市延安西路65号上海国际贵都大饭店办公楼405单元
Phone: +86-21-62489820
Fax: +86-21-62489821

IntechOpen